Electro-optic effect and birefringence in semiconductor vertical-cavity lasers

M. P. van Exter, A. K. Jansen van Doorn and J. P. Woerdman
Huygens Laboratory, University of Leiden, P.O. Box 9504, 2300 RA Leiden, The Netherlands
(Received 3 December 1996)

Semiconductor vertical-cavity surface-emitting lasers (VCSELs) are known to exhibit a small amount of birefringence. We present a model that enables us to estimate how much of this is due to the electro-optic effect produced by the inevitable internal electric field in working devices. Of vital importance for this model is the notion that the position-dependent changes in the refractive index should be weighted by the local optical intensity both in the spacer as well as in the distributed Bragg reflectors. Index variations in the optical nodes thus go unnoticed, whereas those in the antinodes can strongly affect the cavity resonance. This is related to the idea that the active quantum wells in a VCSEL should be positioned in optical antinodes to produce the highest modal gain. The results of our model calculation are compared with statistical data on the magnitude and orientation of the measured birefringence in planar proton-implanted VCSELs. These data show the presence of a systematic contribution to the birefringence, which can presumably be attributed to the electro-optic effect, and a random contribution, which we attribute to stress and strain. [S1050-2947(97)01407-8]

PACS number(s): 42.55.Px, 42.65.Vh

I. INTRODUCTION

An intriguing aspect of semiconductor vertical-cavity surface-emitting lasers (VCSELs) is the polarization of the emitted light. For an ideal VCSEL this polarization is not well defined. For bulk material it is the T_d ($\bar{4}3m$) point group symmetry of the crystal that enforces full rotation symmetry on the linear optical susceptibility [1]. For the common quantum-well structures grown on a [100] substrate it is the S_4 improper rotation along the surface normal that imposes rotational symmetry for the in-plane polarization. Despite these symmetries, practical VCSELs are known to emit linearly polarized light with limited polarization stability [2] and with a weak preference of the polarization orientation for the [110] and [1$\bar{1}$0] crystalline axes [3].

The explanation of the discrepancy mentioned above lies in the occurrence of anisotropies in practical devices [1,4–8]. In several experiments the introduction of intentional anisotropy has been shown to affect the optical polarization. Examples are quantum wells on tilted substrates [1,4], internal ordering in layer design [1] or material choice [5], and elongated transverse VCSEL shapes [6]. Also nominally isotropic VCSELs have been shown to possess (unintentional) anisotropy, mainly in the form of linear birefringence [7,8]. Experimentally, this is easily observable in the optical spectrum of a working VCSEL, which generally contains two TEM_{00} components: a strong lasing mode and a much weaker ''nonlasing'' mode with orthogonal polarization (see the inset of Fig. 1, where the lasing mode has been strongly suppressed with a polarizer). The frequency difference between these modes is a measure for the amount of birefringence, while their polarization orientation gives the axes of the birefringence. These axes are generally close to the [110] and [1$\bar{1}$0] crystalline axes, which themselves correspond to the edges of the chip. Note that we have no *a priori* knowledge which edge corresponds to [110] and which one to [1$\bar{1}$0]; for the time being we will label one chip edge as ''vertical'' and the other as ''horizontal.'' In Sec. VI, however, we will show how the edges can be identified.

Possible mechanisms that can disturb the link between the observed frequency splitting and polarization orientation and the VCSEL's birefringence are deemed to be small. Frequency pulling or pushing of the cavity resonance by a possible detuning of the gain spectrum will be small due to the relatively large spectral width of the latter. The effect of polarization-dependent saturation, related to the existence of two spin channels [9], was in practice also found to be small, i.e., much smaller than the effect of birefringence (see Sec. IV).

The histogram in Fig. 1 shows the measured frequency difference $\Delta\nu$ between the lasing and nonlasing mode for a set of 39 VCSELs. Note that this frequency difference has a sign; we have plotted $\Delta\nu$ and not its absolute value $|\Delta\nu|$.

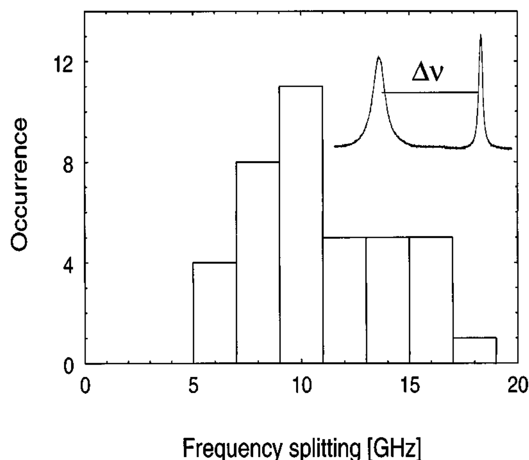

FIG. 1. Histogram of measured frequency splitting between the lasing and nonlasing TEM_{00} modes for a set of 39 VCSELs. As the lasing mode was always more or less ''vertically'' polarized (see the text), this histogram can also be read as the frequency splitting between the ''vertically'' and ''horizontally polarized'' modes. Note the presence of both a systematic and a random component to the birefringence.

 © 1997 The American Physical Society

The frequency difference is found to be positive for all VCSELs of the set. The surprising observation is *not* that the optical frequency of the lasing mode is systematically larger than that of the nonlasing mode; this could be explained by a relative detuning between the cavity resonance and the gain spectrum [10] or by more subtle nonlinear effects [9]. The surprise lies in the observation that the lasing mode is always more or less ''vertically polarized'' and that the *vertically polarized* mode thus always has the largest optical frequency. The underlying birefringence is thus not random and not at all centered around zero as one might have expected. Instead it seems to consist of a systematic contribution of roughly +10 GHz and a random contribution between −5 and 5 GHz. The observation of a systematic contribution to the birefringence was our prime motivation for the present study; although we have recently attributed the random birefringence to strain [7,8], we deemed the presence of a systematic and more or less constant strain unlikely.

Whether a device is optically isotropic or anisotropic depends both on the symmetry of the underlying crystal as well as that of the device structure [1]. More specifically, the in-plane symmetry, imposed by the S_4 improper rotation, can be broken by a device asymmetry in the out-of plane, i.e., the axial, direction. This has recently been discussed and demonstrated for an asymmetric superlattice grading [1,11]. A more natural way in which the out-of-plane device symmetry can be broken is via the internal electric field, which is naturally generated by the space charges and doping in the device. Through the electro-optic effect, which, as a third-order tensor, is not necessarily isotropic in cubic crystals, this axial field will lead to an in-plane electro-optic birefringence. This mechanism, which has been touched upon as a spurious effect in Ref. [11], will be treated extensively in the present paper. The calculation is discussed in Secs. II–V, experimental details are discussed in Sec. VI, and a summary and conclusions are given in Sec. VII.

II. THE ELECTRO-OPTIC EFFECT

Our calculation of the electro-optically induced birefringence in a typical VCSEL consists of three steps: (i) the determination of the internal field $E_{dc}(z)$ as a function of the position z measured perpendicular to the surface, (ii) the calculation of the associated change in refractive index, and (iii) the determination of how this local change affects the cavity resonance frequencies expressed as a modal or spatially integrated birefringence. Step (i) is the most difficult step in the calculation; it will be addressed in Sec. IV. Step (ii) is simple. In crystals without inversion symmetry, such as $Al_xGa_{1-x}As$, the index change induced by a static electric field is commonly described in terms of a linear and quadratic electro-optic effect. For VCSELs grown on a [001] substrate, where the internal electric field thus points in the [001] or vertical direction, the combined action of these effects leads to a change in refractive index of [12]

$$\Delta(1/n^2) = \pm r_{41}E_{dc} + R_{12}E_{dc}^2, \tag{1}$$

where the + and − signs apply to light polarized along the [110] and $[1\bar{1}0]$ directions, respectively. The linear electro-optic effect arises mainly from the Stark shift of atomic core

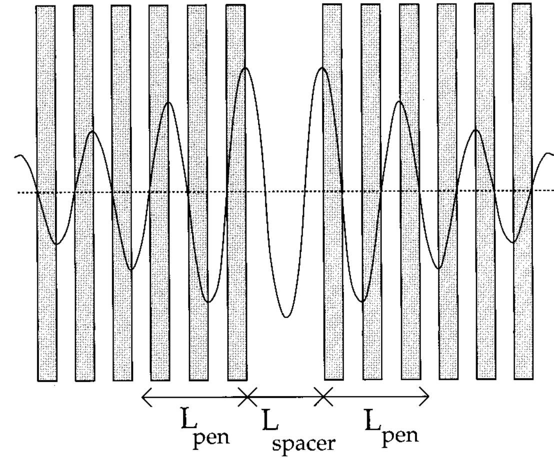

FIG. 2. Sketch of the optical field $\mathcal{E}_0(z)$ in a typical VCSEL. The optical field is approximately a standing wave with an amplitude that is constant over the distance L_{spacer} in between the DBRs and that decays exponentially, with a $1/e$ intensity penetration depth L_{pen}, into the DBRs.

states and its coefficient r_{41} shows hardly any dispersion [12–14]. The quadratic electro-optic effect is linked to electroabsorption and its coefficient R_{12} therefore shows strong dispersion near the band gap [12,13].

We note that the linear electro-optic effect has a different sign for polarizations along the [110] and $[1\bar{1}0]$ axes, whereas the quadratic effect has the same sign, a symmetry that immediately follows from the action of the S_4 improper rotation, which simultaneously interchanges the axes and inverts the electrical field. As the quadratic effect is the same for both polarizations, it drops out of the local birefringence, which becomes

$$n_x(z) - n_y(z) = -n^3(z) r_{41}(z) E_{dc}(z), \tag{2}$$

where x and y denote polarizations along [110] and $[1\bar{1}0]$ and $n(z)$ is the refractive index in zero electric field. The variable z has been introduced to explicitly show the position (read ''material'') dependence of n and r_{41}. The r_{41} coefficient of GaAs is known quite accurately [12–14]; that of $Al_xGa_{1-x}As$ is expected to be almost the same (see Sec. V) [15].

To evaluate how the local birefringence given by Eq. (2) affects the cavity resonance frequency [step (iii) in the calculation], we will need, as explained in Sec. III, the optical field profile $\mathcal{E}_0(z)$ in the VCSEL. Figure 2 shows this profile for a VCSEL comprising two distributed Bragg reflectors (DBRs), composed of materials 2 and 3, with a spacer in between. Due to their limited thickness the presence of quantum wells in the spacer hardly affects the field pattern $\mathcal{E}_0(z)$, which is known to be approximately a standing wave, with constant strength in between the DBRs and with exponentially decaying strength into these mirrors [16,17]. We will denote the thickness of the central cavity as L_{spacer} and the $1/e$ intensity penetration depth into each DBR as L_{pen}. A coupled-mode analysis gives [16]

$$L_{pen} \approx \frac{\lambda_0}{4\,(n_2 - n_3)} = f\frac{\lambda_0}{n_2 + n_3}, \tag{3}$$

where λ_0 is the vacuum wavelength and n_2 and n_3 are the refractive indices in materials 2 and 3, respectively. The factor $f \equiv (n_2+n_3)/4(n_2-n_3)$ corresponds to the number of paired layers (low and high index) over which the standing-wave intensity decays by a factor $1/e$. We have assumed that $n_2-n_3 \ll n_2+n_3$, making $f \gg 1$. The effective cavity length ''felt'' by the optical field is $L_{cav} = L_{spacer}+2L_{pen}$.

At this point we can give a first rough estimate of the electro-optic birefringence. Equation (2) shows that the local birefringence varies with position if $E_{dc}(z)$ does. It seems reasonable to calculate the modal birefringence with the same equation, simply using the spatially average dc electric field $\langle E_{dc} \rangle$ as the ratio of a typical voltage drop over a typical length. We consider a working electrical VCSEL, where the DBRs are n- and p-type doped, respectively. At first sight the voltage drop over this VCSEL is expected to consist of two parts: (i) the voltage drop over the active pn junction, and (ii) the voltage gradient in the DBRs related to the (Ohmic) resistance. In Sec. IV we will argue that the first part is approximately equal to the difference in band gaps of the active and surrounding material $V_{active} \approx V_{gap,2}-V_{gap,1}$, whereas the latter part depends on the voltage drop V_{pair} per DBR pair and the effective number of pairs felt by the optical field. When we choose the positive z axis to point from the n-type towards the p-type DBR the voltage drop over the pn junction is positive (corresponding to a reverse internal field), whereas the voltage gradient over the DBRs will be negative (pointing from the p- to the n-type DBR). A rough estimate of the average dc electrical field $\langle E_{dc} \rangle$ is thus found to be

$$\langle E_{dc} \rangle \approx \frac{V_{active}}{L_{cav}} - \frac{2fV_{pair}}{L_{cav}}. \tag{4}$$

Substitution of Eq. (4) into Eq. (2) using typical values for a VCSEL gives a rough estimate for the electro-optically induced frequency splitting of a few gigahertz.

In Sec. IV we will give a more detailed calculation, which shows that in the simplified treatment given above we have in fact forgotten the most important contribution to the electro-optic birefringence. This contribution stems from the internal fields at the various heterojunctions in the top and bottom DBRs; these DBRs are generally differently doped and this breaks the mirror symmetry with respect to the spacer layer. It did not show up in our rough estimate, as its polarity changes from interface to interface and it thus goes unnoticed in the overall voltage drop. Below, however, we will show how it can strongly affect the cavity resonance once the local birefringence is properly weighted.

III. PERTURBATIVE TREATMENT OF THE OPTICAL WAVE EQUATION

In this section we address step (iii) in the calculation, which is the conversion of the local change in refractive index into a shift of the overall cavity resonance. As the changes induced by E_{dc} are relatively small $n_y-n_x \ll n$, we can profit from the solution $\mathcal{E}_0(z)$ known for $E_{dc}=0$ (see Fig. 2) and expand this result in a perturbative way. We thus apply perturbation theory, which is a standard tool in quantum mechanics [18], to the electro-magnetic wave equation

$$\frac{\partial^2}{\partial z^2}\mathcal{E}(z) + \left(\frac{\omega}{c}\right)^2 \{\epsilon(\omega,z)+\Delta\epsilon(\omega,z)\}\mathcal{E}(z)=0, \tag{5}$$

where the eigenfunction $\mathcal{E}(z)$ is the ''standing wave'' optical field inside the VCSEL, the eigenvalue ω is the cavity resonance frequency, and $\epsilon(\omega,z)$ and $\Delta\epsilon(\omega,z)$ are the (frequency-dependent) dielectric constant at $E_{dc}=0$ and its field-dependent part, respectively. Expansion of $(\omega/c)^2\epsilon(\omega,z)$ around the ''unperturbed'' cavity resonance ω_0 and division of Eq. (5) by $\epsilon(\omega_0,z)$ yields a differential equation that can be dealt with in the standard way. A first-order perturbative treatment of this equation gives the following expression for the shift $(\omega-\omega_0)$ of the cavity resonance:

$$\frac{\omega-\omega_0}{\omega_0} = -\frac{\frac{1}{2}\int dz \frac{\Delta\epsilon(z)}{\epsilon(z)}|\mathcal{E}_0(z)|^2}{\int dz\left\{1+\frac{\omega_0}{2\epsilon(z)}\frac{\partial\epsilon(z)}{\partial\omega}\right\}|\mathcal{E}_0(z)|^2}, \tag{6}$$

where we have dropped the ω index, as all ϵ's should be evaluated at ω_0.

Equation (6) shows that for the shift in resonance frequency the relative variations in ϵ have to be weighted by $|\mathcal{E}_0(z)|^2$; variations of ϵ in the antinodes of the optical field are thus very important, whereas those in the nodes do not count at all. Equation (6) is quite general and can be used for any type of perturbation $\Delta\epsilon(z)$. It shows, for instance, also how the positioning of a quantum-well gain medium with respect to the optical nodes and antinodes is crucial for the modal gain [19,20]; positioning in the anti-nodes maximizes the modal gain, whereas quantum wells in the optical nodes go unnoticed. We use here essentially the same argument for pure index variations induced by a nonzero internal electric field $\mathcal{E}_{dc}(z)$ [see Eq. (2)]. For such pure index variations and $\mathrm{Im}[\epsilon(z)] \ll \mathrm{Re}[\epsilon(z)]$, Eq. (6) reduces to

$$\frac{\omega-\omega_0}{\omega_0} = -\frac{\int dz \frac{\Delta n(z)}{n(z)}|\mathcal{E}_0(z)|^2}{\int dz \frac{n_{gr}(z)}{n(z)}|\mathcal{E}_0(z)|^2}, \tag{7}$$

where $n_{gr}(z)$ is the group refractive index.

In a working VCSEL the internal electric fields will produce opposite shifts of $n_x(z)$ and $n_y(z)$. The resulting shifts of the orthogonally polarized cavity resonances are found by substitution of Eq. (2) into Eq. (7). To simplify the final expression we note that for practical VCSELs the material-dependent quantities $n(z)$,$n_{gr}(z)$, and $r_{41}(z)$ vary only slightly from layer to layer. As these variations are small as compared to the strong position dependence of the standing-wave intensity distribution $|\mathcal{E}_0(z)|^2$, they can, in a reasonable approximation, be substituted by spatially averaged values. We then finally find

$$\frac{\omega_x-\omega_y}{\omega_0} \approx \left\langle \frac{n^3}{n_{gr}} r_{41} \right\rangle \langle E_{dc} \rangle, \tag{8}$$

where the angular brackets denote spatial averaging in the longitudinal direction and we have introduced

$$\langle E_{dc}\rangle \equiv \frac{\int dz E_{dc}(z) I_0(z)}{\int dz I_0(z)} \tag{9}$$

as the average electric field weighted by the local optical intensity $I_0(z) \propto |\mathcal{E}_0(z)|^2$. $\langle E_{dc}\rangle$ proves to be a convenient variable to quantify the electro-optic birefringence. We note that the factorization of averages in Eq. (8) is only approximately correct because the variations in $n(z), n_{gr}(z)$, and $r_{41}(z)$ occur on the same spatial scale as those in $|\mathcal{E}_0(z)|^2$. In principle the original Eq. (7) is thus more accurate, but in practice a further factorization of the material-dependent prefactor in Eq. (8) yields only marginal changes since the variations in $n(z), n_{gr}(z)$, and $r_{41}(z)$ are quite small.

Equations (8) and (9) describe how the local refractive index changes induced by the internal electric field $E_{dc}(z)$ have to weighted by the intensity $I_0(z)$ to evaluate their effect on the overall birefringence and cavity resonance frequency. This weighting procedure is equivalent to the introduction of a ''longitudinal confinement factor'' in the calculation of the effective gain in VCSELs [20]. When this weighting procedure is skipped, as was done in our earlier rough estimate of the electro-optic birefringence, the obtained results could be quite unrealistic.

As discussed in the next section, the dc electric field $E_{dc}(z)$ is generally strongly peaked around the various interfaces. When these variations are localized within a fraction of a wavelength their exact shape is unimportant; what counts is the spatially integrated electric field, i.e., the potential V_{dc}, which is often denoted as the electrostatic or built-in potential

$$\int_{z_0-\delta}^{z_0+\delta} dz E_{dc}(z) I_0(z) \approx V_{dc} I_0(z_0). \tag{10}$$

Below we will calculate these built-in potentials V_{dc} on the basis of the amount of band bending needed to align the Fermi levels in the various materials of the spacer and the DBRs.

IV. INTERNAL ELECTRIC FIELDS

We now return to step (i) in the calculation, which deals with the profiles of the internal electric field $E_{dc}(z)$. This step depends on the device layout, such as material composition and doping levels, and on the external bias needed to produce a certain drive current. Figure 3 sketches the device layout of a generic VCSEL: An active medium, comprising a few (for instance, three) quantum wells of material type 1, is centered in a one-λ cavity of material type 2, which itself is surrounded by DBRs composed of alternating λ/4 layers of material 2 and material 3. The band gaps and refractive indices of materials 1, 2, and 3 will be denoted by $V_{gap,1} < V_{gap,2} < V_{gap,3}$ and $n_1 > n_2 > n_3$, respectively. The various drawn curves in Fig. 3 sketch, in a working VCSEL, the spatial dependence of (a) the conduction band, (b) the upper (heavy hole) valence band, and (c) the internal electric

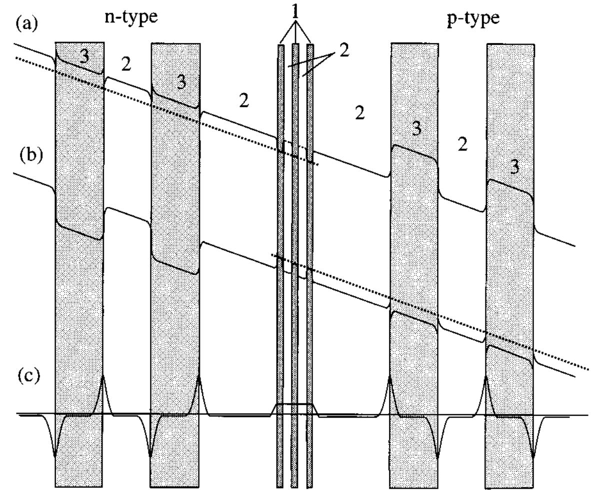

FIG. 3. Sketch of the position dependence of some important quantities in a typical VCSEL, comprising three quantum wells of material type 1 centered in a one-λ cavity of material type 2, which is surrounded by DBRs composed of materials 2 and 3. The various curves show (a) the energy level of the conduction band, (b) the energy level of the upper (hh) valence band, and (c) the internal electric field. The dotted lines in (a) and (b) denote the electron and hole Fermi levels.

field. The Fermi levels in the p- and n-type materials are indicated by the two dotted lines. The slope of the Fermi levels denotes the presence of a uniform series resistance, hindering the enforced drive current. The optical field in the VCSEL was already sketched in Fig. 2.

The internal electric field $E_{dc}(z)$, given as curve (c) in Fig. 3, is no more than a sketch, especially in the neighborhood of the active layer, as the exact field $E_{dc}(z)$ depends critically on the amount and spatial distribution of the doping. The basic physics needed to obtain this curve is quite simple: when two different materials are brought together carrier transport will generally produce charged regions of opposite polarity on both sides of the junction. This space charge results in an internal field across the junction that, in the unbiased case, creates just enough band bending to align the Fermi levels in the different materials and return to equilibrium. This makes the spatially integrated electric field or electrostatic potential equal to the original difference in Fermi levels [21,22].

There are basically three important contributions to the average electric field $\langle E_{\rm dc}\rangle$ and the resulting electro-optic birefringence. These contributions stem from (i) the built-in potential across the active layer, (ii) the series resistance in the device, and (iii) the localized fields at the various DBR heterojunctions.

The first contribution to $\langle E_{dc}\rangle$ arises from the electrostatic potential V_{active} across the active layer. Because the exact profile of $E_{dc}(z)$ on a subwavelength scale does not matter we are allowed to replace the complicated structure of the active layer by a much simpler p-i-n junction, a case that is treated, for instance, in Ref. [22]. In the absence of external bias the alignment of Fermi levels in the doped materials leads to a reverse internal field over the junction and an electrostatic potential that almost equals the band gap of the cladding material 2. For forward bias the Fermi levels in the

p- and n-type material shift with respect to each other and the internal field is reduced. When the external bias and corresponding Fermi level splitting becomes equal to and larger than the band gap of the active material 1, one reaches transparency and than carrier inversion and laser action can occur. In this situation the electrostatic potential over the junction is

$$V_{active}=V_{gap,2}-V_{gap,1}-V_{corr}, \tag{11}$$

where V_{corr} is a small (order 0.05 V) correction that depends on the concentration and binding energy of the dopants, on the quantum-well thickness, and on the degree of inversion in the active medium [22]. Substitution of this potential into Eq. (10) and then back into Eq. (9) shows the contribution of the active layer to $\langle E_{dc}\rangle$ to be

$$\langle E_{active}\rangle=\frac{2\,V_{active}}{L_{cav}}, \tag{12}$$

where the factor of two appears because the active layer is positioned in an optical antinode and the cavity length L_{cav} results from the spatial integral in the denominator of Eq. (9).

The second contribution to $\langle E_{dc}\rangle$ arises from the series resistance of the VCSEL. As this resistance originates dominantly from the relatively thick Bragg mirrors it is most conveniently expressed in terms of the voltage drop V_{pair} per low and high refractive index pair. The magnitude and spatial distribution of the related dc field depends on the material composition and doping of the Bragg mirrors. In the simplest treatment one assumes the series resistance to be uniformly distributed over the DBR, as would be the case for a bulk-type Ohmic resistance. In a more detailed treatment one could separate out the localized Schottky-type resistance associated with tunneling through and thermal emission over the potential barriers at the heterojunctions [23]. However, this introduces several unknowns in the calculation of a contribution that is found to be small anyhow and we will therefore stick to the simple approximation of a uniform series resistance, as sketched in Fig. 3. Given the total number DBR pairs, the magnitude of V_{pair} can be easily obtained from the experimental V-I characteristic of the VCSEL. After substitution into Eq. (9) and spatial integration, which yields a multiplication factor $2f$ as the effective number of DBR pairs felt by the penetrating optical intensity, we get the following expression for the contribution of the series resistance to $\langle E_{dc}\rangle$:

$$\langle E_{series}\rangle=-\,2f\frac{V_{pair}}{L_{cav}}=-\frac{2\,L_{pen}}{L_{spacer}+\,2L_{pen}}\,\frac{V_{pair}}{\lambda_0/(2n)}, \tag{13}$$

where we note that this electric field points towards negative z (from the p- to the n-type DBR), making $\langle E_{series}\rangle<0$.

The third contribution to $\langle E_{dc}\rangle$ arises from the localized fields at the various DBR heterojunctions. These internal fields are of course similar to those appearing at a p-n homojunction. The electrostatic potential across the heterojunction once more depends on the Fermi level difference of the composing materials. However, this now also includes a difference in electron affinity, which is usually quantified by the so-called conduction-band offset η_{CBO}, being the fraction of the band-gap difference that can be assigned to the conduction band [23]. For not too low doping levels the electrostatic potential across each 2-3 heterojunction is equal to $V_{32}\approx V_{gap,3}-V_{gap,2}$ multiplied by η_{CBO} for the n-type DBR and $1-\eta_{CBO}$ for the p-type DBR.

The internal fields at consecutive heterojunctions of a DBR have opposite polarity, pointing away from the high-band-gap material in the n-type DBR and towards it in the p-type DBR (see Fig. 3). At first sight, one might thus expect the contributions of these opposing fields to average out. However, this does not happen as the internal fields have to be weighted by the local optical intensity, which has nodes at one set of heterojunctions and antinodes at the other. Furthermore, the field polarity at the first n-type and first p-type heterojunctions are equal (see Fig. 3). When we now add the contributions to $\langle E_{dc}\rangle$ of the internal fields at the n-type and p-type DBR heterojunction by substituting the potentials mentioned above into Eq. (9), the conduction-band offset η_{CBO} fortunately drops out of the problem. The multiplication factor that occurs due to the spatial integral is $2(f+1/2)$, where the prefactor 2 appears because the potentials are situated in optical antinodes and because the effect of the n- and p-type heterojunctions were already combined and where the term 1/2 appears because the first heterojunctions that count lie already at the boundary of the DBRs. Division by the effective cavity length L_{cav} gives

$$\langle E_{DBRs}\rangle=(\,2f+\,1)\,\frac{V_{32}}{L_{cav}}\approx\frac{\lambda_0/2n+2L_{pen}}{L_{spacer}+2\,L_{pen}}\,\frac{V_{32}}{\lambda_0/2n}. \tag{14}$$

Combining the three contributions given above [Eqs. (12)–(14)] we finally get

$$\begin{aligned}\langle E_{dc}\rangle&=\langle E_{active}\rangle+\langle E_{series}\rangle+\langle E_{DBRs}\rangle\\&=\frac{2V_{active}}{L_{cav}}-\frac{2\,fV_{pair}}{L_{cav}}+\frac{(2\,f+1)V_{32}}{L_{cav}}.\end{aligned} \tag{15}$$

This result differs from the earlier rough estimate [Eq. (4)] by the factor 2 in front of V_{active} and the extra contribution from the DBR heterojunctions. We note that the latter can by very large, mainly because of the multiplication factor $2f+1$, which shows how the electrostatic potentials across the many interfaces add up constructively to a single contribution.

In Sec. V we will find that for practical VCSELs the electro-optic birefringence is by far dominated by the potential across the DBR heterojunctions. This warrants an alternative treatment of this birefringence, in terms of *traveling* instead of *standing* optical waves. For traveling waves the intensity weighting, which was so important before, seems irrelevant. What now becomes important is the phase relation between the forward and backward propagating waves, a phase relation that is imposed by the backscatter from the Bragg gratings and the thickness of the active layer. A convenient way to summarize this backscatter is in terms of the reflection phase $\phi(\omega)$. Well within the stop band the DBR's reflection amplitude is practically constant at almost 100%, whereas its reflection phase $\phi(\omega)$ changes linearly with frequency [17,23]. The point $\phi(\omega)=0$ corresponds to the DBR resonance frequency, where the average optical wavelength

equals twice the grating period; the slope $d\phi(\omega)/d\omega$ is related to the DBR's penetration depth. Below we will show how the electro-optic effect codetermines $\phi(\omega)$ and thereby the cavity resonance frequency.

A simple expression for the reflection phase $\phi(\omega)$ can be obtained from a coupled mode analysis in which the crucial parameter is the coupling rate κ between the forward and backward traveling waves in the DBR [16]. This coupling rate is proportional to the Fourier component of the index variations with the proper $\lambda/2$ periodicity. Inspection of Fig. 3 shows that the index variations originating from the fields across the DBR heterojunctions indeed have this periodicity. However, they are shifted over a $\lambda/4$ period with respect to the primary grating and thus provide a pure imaginary contribution to κ. The result is a shift of $\phi(\omega)$ equal to the ratio of the Fourier components of the electro-optically induced grating and the primary index grating. Mathematically, this shift is equivalent to a (small) detuning of the DBR resonance ω_{DBR} [16] by

$$\frac{\Delta\omega_{DBR}}{\omega_0}=\frac{n}{n_{gr}}\frac{4}{\lambda_0}\int dz\Delta n(z), \tag{16}$$

where the integral applies to a single heterojunction and $\Delta n(z)$ is the electro-optically induced change in refractive index, being negative for one polarization and positive for the other. Substitution of Eq. (2) and integration over z gives the polarization-dependent resonance shift of each DBR in terms of the electrostatic potential over its heterojunctions, which for the n-type and p-type DBR's are proportional to η_{CBO} and $1-\eta_{CBO}$, respectively. The frequency shift of the cavity as a whole is now found by adding these contributions and weighting them with a factor $L_{pen}/(L_{spacer}+2L_{pen})$. When this result is compared with Eq. (8) we find that the internal fields over the DBR heterojunctions contribute to $\langle E_{dc}\rangle$ an amount

$$\langle E_{DBRs}\rangle=\frac{2\,L_{\text{pen}}}{L_{spacer}+2\,L_{pen}}\frac{V_{32}}{\lambda_0/2n}. \tag{17}$$

This result [Eq. (17)], which was obtained for the same field distribution $E(z)$ as used in the perturbative approach, but via a completely different route (traveling versus standing waves), is identical to the result obtained earlier [Eq. (14)] for the practical case of small κ, i.e., large L_{pen}.

V. TYPICAL VALUES TO BE EXPECTED

To get some real numbers for the expected electro-optic birefringence in $Al_xGa_{1-x}As$ structures we start by noting that most quantities in Eq. (8) are rather device independent. At a typical wavelength of 850 nm the refractive indices of $Al_xGa_{1-x}As$ vary, for instance, between about $n\approx 3.0-3.6$ and $n_{gr}\approx 3.5-4.5$ for $x=0-1$. The coefficient r_{41} has only been measured for $x=0$, i.e., GaAs, where it shows practically no dispersion near the band gap and has a value of $r_{41}\approx -1.6\times 10^{-12}$ m/V [12–15]. Unfortunately, there seems to be no established value for r_{41} of AlAs. On the basis of the limited dispersion of r_{41} and the similarity between AlAs and GaP (same number of electrons) it has been argued [15] that one could equally well take the value for GaP, being $r_{41}\approx -1.1\times 10^{-12}$ m/V. This would make the r_{41} coefficient of AlAs about 30% less than that of GaAs, whereas the r_{41} coefficient of $Al_xGa_{1-x}As$ would naturally lie in between. Substitution of $\lambda_0 = 850$ nm and the values for n, n_{gr}, and r_{41} mentioned above into Eq. (8) gives the rather general relation

$$\nu_x-\nu_y\approx\langle E_{dc}\rangle\times 3.0-5.9\ \text{GHz}\ \mu\text{m/V}, \tag{18}$$

where the values 3.0 and 5.9 apply to AlAs and GaAs, respectively, and the frequency splitting $\nu_x-\nu_y$ is expressed in GHz and the average internal field $\langle E_{dc}\rangle$ in V/μm.

We will now concentrate on a special case. In the VCSELs used in our experiment (see Sec. VI) the active layer comprises three GaAs quantum wells centered in a one-λ cavity of $Al_{0.18}Ga_{0.82}As$, whereas the DBRs are composed of alternating $\lambda/4$ layers of $Al_{0.18}Ga_{0.82}As$ and AlAs [24]. We thus have "material 1=GaAs," "material 2=$Al_{0.18}Ga_{0.82}As$," and "material 3=AlAs." At room temperature the respective band gaps are $V_{gap,1}=1.42$ V, $V_{gap,2}=1.67$ V, and $V_{gap,3}=2.17$ V, where the latter corresponds to the indirect gap associated with the X minimum [25]. At the lasing wavelength of 850 nm ($h\nu = 1.46$ eV) the refractive indices of these materials are [25–27] $n_1=3.64$, $n_2=3.46$, and $n_3=2.99$, making $f=3.4$, $L_{pen}=0.45$ μm, $L_{spacer}=0.24$ μm, and $L_{cav}=1.14$ μm. For our $Al_xGa_{1-x}As$ structure, with an average $x\approx 0.59$, the weighted prefactor in Eq. (18) becomes ≈ 4.2 GHz μm/V.

Using the above numbers, we find for the electrostatic potential over the active layer and DBR heterojunctions $V_{active}\approx 0.20$ V and $V_{32}\approx 0.50$ V, respectively. The series resistance is found from the experimental V-I characteristic. At a current of 7 mA, which is 1.4 times above threshold, our VCSELs need typically 2.5 V of external bias. After subtraction of the Fermi level splitting in the active layer ($\approx V_{gap,1}$) and division by the total number of DBR pairs (20+25) we find $V_{pair}\approx 0.024$ V. Substituting these number into Eq. (15) we get the estimate for the electro-optic birefringence

$$\begin{aligned}\nu_x-\nu_y&\approx\Delta\nu_{active}+\Delta\nu_{series}+\Delta\nu_{DBRs}\\&\approx +1.5-0.6+14.4\ \text{GHz}\\&=+15.3\ \text{GHz}.\end{aligned} \tag{19}$$

The above addition, which separates the three different contributions, clearly shows that the electro-optic birefringence must be expected to be dominated by the internal fields at the DBR heterojunctions. As explained above, the effect of these opposing fields does not average out because they should be weighted with the local optical intensity, which has nodes at one set of heterojunctions and antinodes at the other.

TABLE I. Statistical data of the measured birefringence for two types of VCSEL arrays. The mean value and standard deviation of the magnitude and orientation of the birefringence are presented as $\overline{\Delta\nu}$, $\sigma_{\Delta\nu}$, $\overline{\phi}$, and σ_{ϕ}, respectively.

Type of array	Useful lasers	$\Delta\nu$ (GHz)		ϕ (deg)	
		$\overline{\Delta\nu}$	$\sigma_{\Delta\nu}$	$\overline{\phi}$	σ_{ϕ}
1×16	39	10.3	3.3	90.7	3.0
1×8	18	4.1	3.6	89	15

The sign of the above result [Eq. (19)] allows one to distinguish the [110] from the $[1\bar{1}0]$ axis solely on the basis of the optical spectrum emitted by the VCSEL. A positive sign of the result corresponds to light polarized along the [110] axis having a higher resonance frequency than light polarized along $[1\bar{1}0]$ ($\nu_x > \nu_y$).

VI. EXPERIMENTAL RESULTS

We will now return to, and extend, the experimental data presented in Sec. I. In those experiments we have measured, with a polarizer and a planar Fabry-Pérot cavity, the polarization orientation ϕ of the lasing TEM_{00} mode and the frequency splitting $\Delta\nu$ with the other ''nonlasing'' TEM_{00} mode; ϕ and $\Delta\nu$ are associated with the orientation and strength of the birefringence, respectively [7,8]. We have tested 57 different VCSELs located on three 1×16 arrays and three 1×8 arrays. These arrays differed mainly in their pitch (62 versus 125 μm) and size of contact pad (50×50 μm^2 versus 80×80 μm^2) [24]. The proton-implanted devices had emission wavelengths around 850 nm, threshold currents of ≈5.0 mA, and were used at 7.0 mA. The polarization angle ϕ was measured with respect to the array axis, which we assumed to lie exactly along a diagonal crystal axis, being the natural plane of cleavage.

The histogram in Fig. 1 shows the measured values of $\Delta\nu$ for the 1×16 arrays only. Table I summarizes the measured values of $\Delta\nu$ and ϕ for both array types; the accuracy of these measurements is 0.1 GHz for $\Delta\nu$ and 0.5° for ϕ. Figure 4 gives a graphical representation of the data in Table I]; each point ($\Delta\nu$,ϕ) corresponds to one VCSEL, the circles and stars refer to the 1×16 and 1×8 arrays, respectively. The experimental setup was sensitive enough to perform measurements also below the lasing threshold. The (less accurate) values for $\Delta\nu$ and ϕ measured in that situation differed by less than 1 GHz and 2°, respectively, from the above-threshold values. This shows that ''pulling or pushing'' by possible polarization-dependent saturation [9] is small under our experimental conditions. Note that for both array types the birefringence is scattered around a nonzero average magnitude and a well-defined angle $\phi=90°$, which was denoted as ''vertical'' in the Introduction. Note also that we did not use all lasers. On the basis of visual inspection underneath a microscope we rejected devices with deep scratches in the metal contacts or with cracks in the wafer close to the VCSEL. The need for rejection was clearly demonstrated by the extreme values we found for some rejected VCSELs, where we measured, e.g., $\Delta\nu$ =42 GHz and ϕ = 60°.

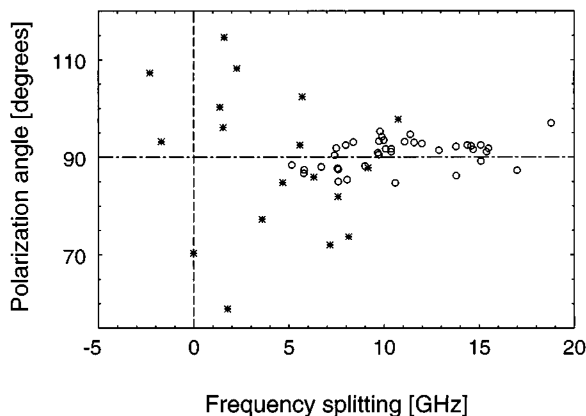

FIG. 4. Scatter plot of the magnitude and orientation of the measured birefringence for the VCSELs from the 1×16 arrays (open circles) and those from 1×8 arrays (stars).

We believe that the observed average or systematic birefringence is to a large extent due to the electro-optic effect, whereas the random birefringence (or spread in $\Delta\nu$ and ϕ) is related to random stress and strain in combination with the elasto-optic effect [7,8]. For all lasers the polarization direction showed a strong preference for the angle $\phi=90°$, being perpendicular to the array axis and thus along a diagonal crystal axis ([110] or $[1\bar{1}0]$). This agrees well with the preference predicted for the electro-optic effect. In the absence of any other anisotropies this polarization is expected to be exactly identical for all lasers. In practice strain will spoil the perfect directionality (see below).

The observation that $\Delta\nu>0$, i.e., that the frequency of the ''vertically polarized'' lasing mode is larger than that of the ''horizontally polarized'' nonlasing mode, allows us to discriminate the [110] from the $[1\bar{1}0]$ direction. A comparison with the sign of the predicted electro-optic birefringence leads us to conclude that in our VCSELs the ''vertical direction'' corresponds with the [110] crystal axis. The array axis, which is orthogonal to this direction, must thus be aligned along the $[1\bar{1}0]$ crystal axis. This information is difficult to obtain otherwise; without the manufacturer's help one has to rely on Röntgen diffraction on the mounted device or other, destructive techniques.

For the lasers from the 1×16 arrays we measured an average frequency splitting $\overline{\Delta\nu}\approx+10$ GHz; for the lasers from the 1×8 arrays we found $\overline{\Delta\nu}\approx+4$ GHz. These values seem to be somewhat small, but are of the same order of magnitude as the +15 GHz predicted for the electro-optic birefringence. It is not yet clear why there is a difference between the two array types. Unfortunately, we cannot rule out other systematic contributions to the birefringence, a possible candidate being systematic strain arising from the nonuniform environment of VCSELs in an array due to the presence of neighboring lasers and nearby electrical contacts. Still, we consider the observed systematic birefringence and the order-of-magnitude agreement with theory a strong indication for the existence of an electro-optic birefringence in practical VCSELs. However, the evidence is not conclusive

and it would be very interesting to compare our theoretical prediction with experimental data for other VCSELs, preferably produced via different techniques.

As a bonus of the statistical data presented in Fig. 4 and Table I, we will now analyze the observed *spread* in birefringence to obtain information about the generating stress and strain in the devices. The relation between birefringence and stress has been studied quite extensively in another experiment, where a controllable amount of stress was added by means of local heating in the vicinity of the VCSEL [7,8]. That relation was measured to be highly anisotropic: When stress was applied along the [110] or [1$\bar{1}$0] axis the resulting birefringence was a factor $A_{eo}/A_{el} \approx 2.7 \pm 0.5$ larger than when the same amount of stress was applied along the [100] or [010] axis, A_{eo} and A_{el} being the elasto-optic and the elastic anisotropy factor, respectively. The combination of this result with the known value $A_{el} = 1.8$ gave an even larger anisotropy of $A_{eo} \approx 4.9 \pm 0.7$ for the relation between strain and birefringence [7,8].

The statistical data in Table I allows us to deduce information on the anisotropy of the elasto-optic tensor. Even when the underlying stresses or strains are assumed to be randomly distributed in angle and strength, the resulting birefringence will show a preference for the diagonal axes. For random stress we expect an anisotropy of $A \approx 2.7$; for random strain we expected $A \approx 4.9$. To get a statistical estimate of the experimental anisotropy A_{stat}, using the assumption of random stress or strain, we note that the systematic and random birefringence add in a tensorial way [7,8]. When the random birefringence is much smaller than the systematic one this addition simplifies considerably and the statistically determined anisotropy factor A_{stat} is found to be

$$A_{stat} = \frac{\sigma_{\Delta\nu}}{2\,\Delta\nu_{av}\sigma_{\phi}}, \tag{20}$$

where $\sigma_{\Delta\nu}$, σ_{ϕ}, and $\Delta\nu_{av}$ are the spread in $\Delta\nu$, the spread in ϕ, and the average frequency splitting, respectively.

When we apply the above recipe to the data from the 1×16 arrays, for which the condition $\sigma_{\Delta\nu} \ll \Delta\nu_{av}$ applies, we obtain $A_{stat} \approx 3.1$. For the 1×8 arrays, where $\sigma_{\Delta\nu} \approx \Delta\nu_{av}$, the tensor addition should be performed to higher order in $\sigma_{\Delta\nu}/\Delta\nu_{av}$, yielding an extra factor $\sqrt{1 + 2(\sigma_{\Delta\nu}/\Delta\nu_{av})^2}$ on the right-hand side of Eq. (20). Substitution of the statistical data for 1×8 array now gives a rough estimate of $A_{stat} \approx 2.7$. The two estimates given above are comparable to the value $A_{eo}/A_{el} \approx 2.7 \pm 0.5$ as determined from earlier, more direct, experiments [7,8]. They thus seem to confirm both the high anisotropy of the elasto-optic effect as well as the assumption of random stress.

We note that the random birefringence measured for the two array types is approximately the same. This is demonstrated by the values of $\sigma_{\Delta\nu}$ in Table I, which are practically the same for both arrays. It is also demonstrated by the unequal values of σ_{ϕ}; although the polarization orientation of the VCSELs from the 1×16 arrays is much better defined, this is only so because of the larger systematic birefringence in these lasers, which makes the polarization rotation induced by the random birefringence relatively less important. The anisotropy of the elasto-optic tensor in fact helps to even further reduce the spread σ_{ϕ} [see Eq. (20)].

VII. SUMMARY AND CONCLUSIONS

In summary, we have discussed how the internal electric fields in a working VCSEL result in electro-optic birefringence. We have quantified the various contributions to this birefringence and shown that the largest effect generally comes from the internal electric fields at the heterojunctions in the DBR mirrors. A key point in the calculation was the idea that these fields have to be weighted by the local optical intensity, which exhibits nodes and antinodes at consecutive heterojunctions. An estimate of the electro-optic birefringence in a typical VCSEL leads to an expected frequency splitting between the orthogonally polarized TEM_{00} modes of about 15 GHz.

Statistical analysis of measurements on a set of 57 VCSELs shows the experimental birefringence to be composed of a systematic and a random contribution. The systematic birefringence is ascribed to the electro-optic effect, maybe in combination with other causes, whereas the random birefringence is ascribed to random stress and strain. The systematic birefringence was found to be oriented along the [110] axis, its magnitude being comparable to the predicted value. A comparison between the observed variations in frequency splitting and polarization angle ($\sigma_{\Delta\nu}$ and σ_{ϕ}) confirmed earlier claims that the elasto-optic tensor is highly anisotropic. We predict that any reduction of the random birefringence will automatically lead to a more reproducible VCSEL polarization since in that case a more dominant role will be played by the electro-optic birefringence that is inherent in the standard VCSEL design and that has a well-defined direction and magnitude.

We note that the predicted electro-optic birefringence stems from voltage drops and is therefore not directly linked to current. The effect can thus equally well occur in optically pumped VCSELs, at least when they contain asymmetric doping, i.e., p-type doping for one DBR and n-type doping for the other DBR. In wafers with such standard doping a calculation along the lines sketched above will give comparable values for $\langle E_{dc} \rangle$ and the electro-optic birefringence. The only way to avoid electro-optic birefringence is to use fully symmetric devices, such as undoped wafers or symmetrically doped wafers (pp or nn), where the electro-optic effects disappear in the spatial average. This idea has been confirmed in a recent study of optically pumped VCSELs, where the birefringence in a standard-doped pn wafer was found to be about 10 GHz, whereas it was practically absent (<2 GHz) for a symmetrically doped pp wafer [28].

ACKNOWLEDGMENTS

We thank Vixel Corporation for kindly supplying us the special arrays needed for the experiment. We acknowledge support of the ''Stichting voor Fundamenteel Onderzoek der Materie'' and of the European Union in ESPRIT Project No. 20029 (ACQUIRE) and TMR Network No. ERB4061 PL951021 (Microlasers and Cavity QED). The research of M.P.v.E. has been made possible by the ''Royal Netherlands Academy of Arts and Sciences.''

[1] D. Vakhshoori, Appl. Phys. Lett. **65**, 259 (1994).
[2] K. D. Choquette and R. E. Leibenguth, IEEE Photonics Technol. Lett. **6**, 40 (1994).
[3] C. J. Chang-Hasnain, J. P. Harbison, L. T. Florez, and N. G. Stoffel, Electron. Lett. **27**, 163 (1991).
[4] T. Ohtoshi, T. Kuroda, A. Niwa, and S. Tsuji, Appl. Phys. Lett. **65**, 1886 (1994).
[5] A. T. Meney, E. P. O'Reilly, and K. J. Ebeling, Electron. Lett. **31**, 641 (1995).
[6] T. Yoshikawa, H. Kosaka, M. Kajita, K. Kurihara, Y. Sugimoto, and K. Kasahara, Electron. Lett. **31**, 1573 (1995).
[7] A. K. Jansen van Doorn, M. P. van Exter, and J. P. Woerdman, Appl. Phys. Lett. **69**, 1041 (1996).
[8] A. K. Jansen van Doorn, M. P. van Exter, and J. P. Woerdman, Appl. Phys. Lett. **69**, 3635 (1996).
[9] M. San Miguel, Q. Feng, and J. V. Moloney, Phys. Rev. A **52**, 1728 (1995).
[10] K. D. Choquette, R. P. Schneider, Jr., K. L. Lear, and R. E. Leibenguth, IEEE J. Sel. Topics Quantum Electron. **1**, 661 (1995).
[11] D. Vakhshoori and R. E. Leibenguth, Appl. Phys. Lett. **67**, 1045 (1995).
[12] J. Faist and F. K. Reinhart, J. Appl. Phys. **67**, 6998 (1990); **67**, 7006 (1990).
[13] C. A. Berseth, C. Wuethrich, and F. K. Reinhart, J. Appl. Phys. **71**, 2821 (1992).
[14] S. Adachi, J. Appl. Phys. **72**, 3702 (1992).
[15] M. Glick, F. K. Reinhart, and D. Martin, J. Appl. Phys. **63**, 5877 (1988).
[16] H.A. Haus, *Waves and Fields in Optoelectronics* (Prentice-Hall, Englewood Cliffs, NJ, 1984), Chap. 8.
[17] D. I. Babic, Y. Chung, N. Dagli, and J. E. Bowers, IEEE J. Quantum Electron. **29**, 1950 (1993).
[18] E. Merzbacher, *Quantum Mechanics* (Wiley, New York, 1970), Chap. 17.
[19] M. Y. A. Raja, S. R. J. Brueck, M. Osinski, C. F. Schaus, J. G. McInerney, T. M. Brennan, and B. E. Hammons, Electron. Lett. **24**, 1141 (1988).
[20] S. W. Corzine, R. S. Geels, J. W. Scott, R.-H. Yan, and L. A. Coldren, IEEE J. Quantum Electron. **25**, 1513 (1989).
[21] S. S. Li, *Semiconductor Physical Electronics* (Plenum, New York, 1993), Chap. 11.
[22] H. C. Casey, Jr. and M. B. Panish, *Heterostructure Lasers, Part A: Fundamental Principles* (Academic, Orlando, 1978).
[23] T. E. Sale, *Vertical Cavity Surface Emitting Lasers* (Wiley, New York, 1995).
[24] Prototype devices from Vixel Corporation, 325 Interlocken Parkway, Broomfield, CO 80021.
[25] J. S. Blakemore, J. Appl. Phys. **53**, R123 (1982).
[26] D. E. Aspnes, S. M. Kelso, R. A. Logan, and R. Bhat, J. Appl. Phys. **60**, 754 (1986).
[27] R. E. Fern and A. Onton, J. Appl. Phys. **42**, 3499 (1971).
[28] R. F. M. Hendriks, M. P. van Exter, and J. P. Woerdman (unpublished).